

¹ **Topographic resolution impacts the global
overturning in realistic ocean GCMs**

Maike Sonnewald,^{1,2}

Joël J.-M. Hirschi³, A. George Nurser³, Andrew Coward³, Patrick Hyder⁴

Corresponding author: Maike Sonnewald, Harvard University, 26 Oxford Street, Cambridge, MA 02138. (maike_s@mit.edu)

¹Massachusetts Institute of Technology,
77 Massachusetts Ave, Cambridge, MA
02139, USA.

²Harvard University, 26 Oxford Street,
Cambridge, MA 02138.

³National Oceanography Centre,
Southampton,European Way, Southampton
SO14 3ZH, UK

⁴Met Office, FitzRoy Road, Exeter EX1
3LX, UK

3 Abstract.

4 Realistic ocean models are pushing the computational limits of horizon-
5 tal resolution, with significant changes to ocean dynamics left uncharacter-
6 ized. Theoretical understanding of ocean physics is largely based on a lam-
7 inar view of the ocean, assuming the non-linear vorticity terms are small. An
8 assessment of the change in dynamics with resolutiuon in a decadal (30 year),
9 climate relevant, and realistic ocean model is presented. A coarse (1°), eddy
10 permitting ($1/4^\circ$) and eddy resolving ($1/12^\circ$), version of the NEMO general
11 circulation model is used, and the time mean shows that the baroclinic con-
12 tribution to the meridional overturning becomes increasingly important with
13 higher resolution, especially in the Southern Ocean. This highlights the dif-
14 ferent mechanisms active for meridional transport when eddies are resolved.
15 Using the depth integrated vorticity equation, the change is ascribed to eddy
16 contributions to the bottom pressure torque term. This suggests a fundamen-
17 tal change in how the circulation is realized, with important implications for
18 the fidelity and utility of ocean modeling efforts where the global redistribu-
19 tion of heat on decadal timescales is important such as for climate stud-
20 ies used in the IPCC report.

21

1. Motivation

Realistic ocean models are seminal in offering insight into ocean dynamics. Global ocean general circulation models (GCMs) are a critical for future projections of changes in e.g. heat, carbon or salt, acting as the link between ocean observations and theory. Understanding mechanisms at play is the basis of successful projection under changing boundary conditions. Crucially, changing horizontal resolution in ocean GCMs are linked to increased accuracy [Megann *et al.*, 2014, @; Marzocchi *et al.*, 2015, @; Marsh *et al.*, 2009, @], and reduced bias in climate models [Scaife *et al.*, 2011, @] compared to observations. Resolving the dynamical roles of eddies explicitly is credited with this success [Schoonover *et al.*, 2016, @]. A systematic assessment of the role of resolution in realistic GCMs is presented, focusing on the meridional overturning and examining changes.

32

Understanding how eddies interact with bathymetry is important as it determines how meridional transport is realized and Ψ is impacted. Two extremes exist:

$$\underbrace{f \frac{\Delta H}{H} >> \beta}_{\text{Rough topography, little bottom flow}} \quad \stackrel{\text{Most ocean GCMs}}{\Leftrightarrow} \quad \underbrace{f\text{-contours}}_{\text{Flat bottom}}.$$

On the RHS, the sea floor is flat, and the flow follows contours of the Coriolis parameter (f -contours). On the LHS, flow at the bottom is slight and topography (H) is so rough ∇H takes over. Realistic ocean physical regimes are largely on the spectrum between these extremes. Unpicking what drives the meridional flow, previous work has focused on the barotropic (depth integrated) vorticity (BV) equation, demonstrating a strong connection between the overturning and gyre circulation examined using the bottom pressure torque term ($BPT; J(p_b, H)$) [Yeager, 2015, @; Schoonover *et al.*, 2016, @]. The BPT term can

40 be broken down into a barotropic and baroclinic component, which was demonstrated by
 41 Yeager, 2015 [@[to allow for a distinction between the overturning and gyre contribution
 42 of the BPT:

$$\frac{1}{\rho_0} J(p_b, H) = f \mathbf{u}_{gb} \cdot \nabla H = \overbrace{f(\mathbf{u}_{gb} - \bar{\mathbf{u}}_g) \cdot \nabla H}^{\text{Baroclinic: JEBAR}} + \overbrace{f \bar{\mathbf{u}}_g \cdot \nabla H}^{\text{Barotropic}}. \quad (1)$$

43 Where u_g is the horizontal *geostrophic* velocity, with the overbar indicating the depth
 44 average, and u_{gb} is the same evaluated at the bottom. The joint effect of baroclinicity
 45 and relief (JEBAR) was discussed critically by Cane *et al.*, 1998 [@[due to e.g. spurious
 46 cancellation. Its utility is discussed to highlight where the term can usefully be applied.
 47 Recognizing what ranges of physical regimes and scales are appropriate when harnessing
 48 a model's skill is key for assessing impacts on quantities like the global overturning.

49
 50 Interactions between steep bathymetry and the circulation impact the BV balance, with
 51 the deep flow associated with the heat flux forcing [Yeager, 2015, @; Luyten *et al.*, 1985,
 52 @]. Studies by Schoonover *et al.*, 2016 [@[; Yeager, 2015 [@[; Hughes and de Cuevas,
 53 2001 [@[; Jackson *et al.*, 2006 [@[; Wells and de Cuevas, 1995 [@[highlight the role of
 54 bottom pressure torque in balancing the wind stress, in opposition to the classical models
 55 of Stommel, 1948 [@[; Munk, 1950 [@[. The importance of abyssal flow interactions with
 56 bathymetry has implications for modeling efforts, as the ∇H term (Eq. 1) changes with
 57 resolution. Modeling choices of resolution and parameterization are seen to impact the
 58 nature of how the ocean realizes its circulation, and achieving good representations of fric-
 59 tional and viscous effects (both explicit and numerical) is important for key features such
 60 as the western boundary current (WBC) separation and the global overturning [Yeager,

₆₁ 2015, @; Schoonover *et al.*, 2016, @].

₆₂

₆₃ The large scale circulation can be understood in terms of an acceleration due to wind
₆₄ stress (τ_w), and a deceleration due to pressure forces exerted by bathymetry (τ_b) [Sver-
₆₅ drup, 1947, @; Stommel and Arons, 1960a, @; Stommel and Arons, 1960b, @]. Forces
₆₆ like the BPT act to redistribute rather than dissipate. The horizontal gyre circulation
₆₇ is commonly discussed using vorticity arguments, while the Southern Ocean is discussed
₆₈ in terms of momentum. The Southern Ocean is of particular interest due to its lack of
₆₉ western boundaries implies that the Southern Ocean is governed by another mechanism.
₇₀ No simple linear model has gained acceptance in literature [LaCase and Isachsen, 2010,
₇₁ @]. Munk and Palmén, 1951 [@] suggest that the wind stress is balanced by bottom
₇₂ friction, as the ACC interacts with H in key regions. As Wells and de Cuevas, 1995 [@]
₇₃ discuss, the stratification and explicit representation of eddies is important for the vertical
₇₄ transport of stress from the surface to depth, and the creation of bottom form drag. In
₇₅ the Southern Ocean, the meridional components of the ACC span sufficient depth to allow
₇₆ communication of stresses from surface to bottom. The mechanism suggested by Munk
₇₇ and Palmén, 1951 [@] would be highly sensitive to changes in the horizontal resolution
₇₈ through changes in the ∇H as well as the surface to depth communication enabled by
₇₉ resolving smaller scales.

₈₀

₈₁ The goal of our study is a systematic comparison of changes in decadal dynamics in
₈₂ realistic ocean GCMs. Focus is on the meridional overturning (Ψ) and interactions of the
₈₃ horizontal flow with H. Examining changes when moving from realistic ocean GCMs at

84 non-eddying (1°), intermediate ($1/4^\circ$) to eddy-permitting resolution ($1/12^\circ$), this study
 85 examines decadal responses in Ψ to characterize changes associated with H to through
 86 allowing increased baroclinic activity.

87

2. Methods

88 The setup of the realistic ocean model GCM where three horizontal resolutions explore
 89 the non-eddy resolving, intermediate to eddy-permitting was the product of a DRAKKAR
 90 meeting, with the setup rooted in the expertise of the authors and present committee.
 91 The Nucleus for European Modeling of the Ocean (NEMO, Madec, 2008 [@] in the ORCA
 92 configuration) over 30 years (1978 to 2007) is used. The z-level model uses an Arakawa
 93 C-grid with 75 vertical levels and horizontal resolution ranging from 1° (ORCA1), $1/4^\circ$
 94 (ORCA025) and $1/12^\circ$ (ORCA0083). The suite of runs is kept as similar as possible,
 95 while conserving numerical stability. A leapfrog timestepping scheme is used to reduce
 96 noise [Arakawa and Lamb, 1977, @]. The surface layer is allowed to vary and we use a
 97 non-linear free surface scheme. The equation of state used is Jackett and McDougall, 1995
 98 [@]. Analysis is performed on 5 day averages, while the timestep in the model forcing
 99 is 6 hourly using the forcing DFS4.1 [Brodeau *et al.*, 2010, @] for all three runs. The
 100 ice model is the LIM sea-ice model. Tides and geothermal heating are not included,
 101 but a diffusive, nonlinear friction, bottom boundary layer scheme is active. The bottom
 102 diffusivity parameters stay constant at $1000\ m^2 s^{-1}$ in the different resolutions. Further,
 103 noise is reduced using an energy-enstrophy conserving scheme for momentum advection
 104 in combination with using partial cells at the bottom. The bathymetry of the 1° , $1/4^\circ$ to
 105 $1/12^\circ$ are described in Coward, 2006 [@], Barnier *et al.*, 2006 [@] and Bourdallé-Badie *et*

¹⁰⁶ *al.*, 2012 [@[], respectively.

¹⁰⁷

¹⁰⁸ Table 1 lists key parameters that change with the resolution. At 1° ORCA1, the ad-
¹⁰⁹ dition of GM, calculated from the local growth rate of baroclinic instabilities, acts to
¹¹⁰ adjust the advective formulation. The horizontal laplacian eddy viscosity decreases from
¹¹¹ $1.25 \times 10^{10} m^4 s^{-1}$ in ORCA1 to $500 m^4 s^{-1}$ in ORCA025 and ORCA0083. The horizontal
¹¹² bilaplacian eddy viscosity decreases from $1.25 \times 10^{10} m^4 s^{-1}$ in ORCA1 to $2.2 \times 10^{11} m^4 s^{-1}$
¹¹³ in ORCA025 and ORCA0083. The lateral eddy tracer diffusivity decreases consistently
¹¹⁴ from $10^3 m^2 s^{-1}$ in ORCA1 to $300 m^2 s^{-1}$ in ORCA025 and $125 m^2 s^{-1}$ in ORCA0083. Pa-
¹¹⁵ rameters associated with the turbulent kinetic energy (TKE) scheme, Richardson number
¹¹⁶ dependent vertical diffusion or vertical physics do not change with resolution because
¹¹⁷ the vertical resolution does not change. However, these are velocity dependent, and may
¹¹⁸ behave differently between resolutions even though the parameters are kept fixed.

¹¹⁹

¹²⁰ To assess changes in the global circulation, we use the meridional overturning stream-
¹²¹ function Ψ_σ in density space (σ , referenced to 2000m) as described in Zika *et al.*, 2012 [@[];
¹²² Nurser and Lee, 2004 [@[].

$$\Psi_{\sigma y} = \frac{1}{\Delta t} \int_t^{t+\Delta t} \int \int_{\sigma' \leq \sigma} v dx dz dt. \quad (2)$$

¹²³ Ψ is decomposed into barotropic (BT: \bar{v}) and baroclinic (BC: v') components:

$$\begin{aligned}\Psi_{\sigma y}^{BC} &= \int \int_{\sigma' \leq \sigma} v' dx dz, \\ \Psi_{\sigma y}^{BT} &= \int \int_{\sigma' \leq \sigma} \bar{v} dx dz, \\ \Psi_{\sigma y} &= \Psi_{\sigma y}^{BC} + \Psi_{\sigma y}^{BT}.\end{aligned}\quad (3)$$

₁₂₄ Where $v = \bar{v} + v'$, and $\bar{v} = \frac{1}{H} \int_{-H}^0 v dz$ and $v' = v - \bar{v}$.

₁₂₅

₁₂₆ Understanding the changes in Ψ , the BV equation is a useful simplification of the full
₁₂₇ momentum equations that make up its constituent terms. A derivation of the BV equa-
₁₂₈ tions where the BPT arises is available in e.g. Hughes and de Cuevas, 2001 [@], while the
₁₂₉ appendix covers the derivation of the JEBAR term. For the unfamiliar reader, developing
₁₃₀ an intuition for the BPT term is covered in the appendix. The discussion will focus on
₁₃₁ the implication for Ψ of the BPT and the component the JEBAR term makes up as seen
₁₃₂ in Eq. 1.

₁₃₃

₁₃₄ To objectively compare the representation of ∇H and BPT at the different model
₁₃₅ resolutions we define a probability density function (PDF) for both quantities:

$$PDF(\phi) = \lim_{\Delta\phi \rightarrow 0} \left(\iint_A \phi - \Delta\phi < \phi < \phi + \Delta\phi dA \right) / \iint_A \phi dA, \quad (4)$$

₁₃₆ where ϕ stands for absolute values of either ∇H or BPT. $PDF(\phi)$ is then the probability
₁₃₇ that the value of ϕ lie between $\phi - \Delta\phi$ and $\phi + \Delta\phi$ (i.e. the fraction of values of ϕ that
₁₃₈ fall within this range). The definition of Eq. 4 also ensures that the cumulative density
₁₃₉ function (CDF) fulfills the requirement for unity when integrating over all PDF values i.e.

$$\int_{\phi_{min}}^{\phi_{max}} PDF(\phi) d\phi = 1, \quad (5)$$

140 where ϕ_{min}, ϕ_{max} are the minimum and maximum bin values. Using Eq. 4 allows a fair
 141 comparison of terms irrespective of area covered, as “smoothing” over larger areas could be
 142 thought to lead to conformity among the model runs through cancellations in the higher
 143 resolution.

144

3. Results

145 Increasing the horizontal resolution increases the roughness of H in the ocean GCM.
 146 Fig. 1 illustrates in the top row of global maps of ∇H that this has a distinct pattern.
 147 The shelf is outlined around the continents, especially in the non-eddy resolving 1° resolu-
 148 tion. Vast expanses of ocean bathymetry appear smooth in the non-eddy resolving 1° , in
 149 contrast to the intermediate $1/4^\circ$ and eddy-permitting $1/12^\circ$ resolution. We can see the
 150 outline of the Atlantic Ridge, as well as the Pacific-Antarctic and the Southwest Indian
 151 Ridge. The fracture zones in the Southern Ocean are visible as orthogonal streaks to
 152 the ridge structures, specifically the Eltanin and Udintsev fracture zones on the Pacific-
 153 Antarctic Ridge. The Drake Passage and Scotia Ridge area are associated with dramatic
 154 bathymetry, with increasing steepness with resolution. The Weddell Gyre region can be
 155 seen as a reasonably cut-off area in terms of bathymetry. For the intermediate $1/4^\circ$ res-
 156 olution more detail appears in ∇H , features are visible in the interior particularly over
 157 regions of known rough bathymetry. In the eddy-permitting $1/12^\circ$ resolution there is a
 158 marked increase in roughness, with isolated “hotspots”.

159

¹⁶⁰ The middle row in Fig. 1 shows the latitudinal PDFs as defined in Eq. 4, interpreted
¹⁶¹ as in looking down on a histogram for each latitude. The PDFs show a sharply peaked
¹⁶² distribution at 1° resolution, where the tropical mesh refinement offers a demonstration
¹⁶³ of increasing the resolution smoothly to $1/3^\circ$. Increasing the resolution, the skew of the
¹⁶⁴ distribution decreases, and the PDFs widen. This is done for the global (Fig. 1 bottom
¹⁶⁵ plot) as well as the longitudinal averages. All resolutions demonstrate that most of the
¹⁶⁶ ocean floor is fairly smooth, with low values of ∇H dominating spatially. The steep
¹⁶⁷ slopes tend to cluster around discrete values, which illustrates that the slopes are largely
¹⁶⁸ similar irrespective of the basin. Steeper slopes are found with increasing resolution as
¹⁶⁹ expected; the eddy-permitting $1/12^\circ$ resolution clusters around higher values, a tendency
¹⁷⁰ which increases towards the higher latitudes. This is expected due to the higher number
¹⁷¹ of gridpoints. The intermediate $1/4^\circ$ resolution also has higher values, but more concen-
¹⁷² trated towards lower bins. In the plots of longitudinal averages there are streaks of higher
¹⁷³ probability which are set by the resolution, changing with latitude.

¹⁷⁴
¹⁷⁵ Fig. 2 shows the 30 year zonal mean $\Psi_{\sigma y}$ as defined in Eq. 2 and 3 for the full (top
¹⁷⁶ row), barotropic (middle row) and baroclinic (bottom row) cases, with the columns rep-
¹⁷⁷ resenting the ocean GCM resolutions. The increase in the counterclockwise (blue) mean
¹⁷⁸ circulation in the Southern Ocean with resolution is striking. The lighter equatorial waters
¹⁷⁹ show the big wind-driven gyres, while waters get increasingly dense moving polewards,
¹⁸⁰ lending the figures the bell-shape. At $\approx 52^\circ\text{N}$ the North Atlantic deep water (NADW)
¹⁸¹ is visible. Spreading from the high latitudes in the Southern Hemisphere, the Antarctic
¹⁸² bottom water (AABW) spreads northward. The deep circulation in the Southern Ocean

¹⁸³ and its northward extension, as well as the NADW cell, are significantly strengthened
¹⁸⁴ with increasing resolution. The equatorial and subtropical cells are similar, and intensify
¹⁸⁵ with increasing resolution.

186

¹⁸⁷ Following Eq. 3 the 30 year time mean overturning $\Psi_{\sigma y}$ is decomposed into barotropic
¹⁸⁸ and baroclinic components in the bottom row of Fig. 2. There is a clear compensat-
¹⁸⁹ ing pattern, where a clockwise circulation in one will be mirrored by a counterclockwise
¹⁹⁰ component in the other. The barotropic component is seen to often counter the direction
¹⁹¹ of the baroclinic, with the opposite signs leading to compensating transports. Absolute
¹⁹² overturning values are markedly smaller for the full overturning than for the barotropic
¹⁹³ and baroclinic components. The baroclinic component contains the wind driven gyre fea-
¹⁹⁴ ture in the lighter, low latitude waters, as well as the clockwise component of the NADW.
¹⁹⁵ The anti-clockwise component in the Southern Ocean is primarily found in the baroclinic
¹⁹⁶ component. The make up of AABW and NADW cells change with latitude with e.g. the
¹⁹⁷ northernmost part of the NADW cell being dominated by the baroclinic component, whilst
¹⁹⁸ further south (between 20-40°N) the barotropic component dominates. Fig. 2 illustrates
¹⁹⁹ that the increase in anti-clockwise circulation in the Southern Ocean can be accounted
²⁰⁰ for by the baroclinic circulation. We see a clockwise dense circulation in the Southern
²⁰¹ Ocean in the barotropic mean, extending northward and into lighter water masses with
²⁰² increasing resolution. Overall, in the subtropics, we see a strengthening of the subtrop-
²⁰³ ical circulation with decreasing resolution. However, the anti-clockwise WBCs become
²⁰⁴ increasingly well defined with resolution in the Southern Hemisphere. Further changes in
²⁰⁵ the Northern Hemisphere include a strengthening of the NADW with resolution, and a

206 weakening of the baroclinic anti-clockwise subtropical circulation. In the baroclinic mean,
207 the clockwise WBCs in the Northern Hemisphere become better defined and span a wider
208 range of densities with increasing resolution. The patterns in the Southern Ocean are
209 striking, and will be the focus of the subsequent discussion.

210

211 The BPT term changes significantly with resolution in the 30 year mean, particularly
212 becoming more pronounced around areas of rough H as seen in the top row of Fig. 3.
213 The non-eddy resolving 1° demonstrates that significant BPT is found in the shelf regions
214 and regions of steep bathymetry, such as the Scotia Ridge, the Kerguelen Plateau and the
215 Northern Mid-Atlantic Ridge. A physically intuitive pattern of positive (negative) BPT
216 to the East of a topographic feature, and negative (positive) to the West for eastward
217 (westward) flow. This can be interpreted as the flow converging as it hits the obstacle
218 and diverging after, leading to vortex squishing initially, and vortex stretching after. For
219 the intermediate resolution $1/4^\circ$ the BPT patterns are similar in terms of highlighting
220 shelf regions and rough bathymetry, but regions are locally more confined to smaller ar-
221 eas on the shelf. Patterns of negative/positive values in response to topographic barriers
222 are seen. Areas where the BPT is significant are more widespread, and the Northern
223 Mid-Atlantic Ridge down to the Equator, as well as the Pacific-Antarctic Ridge and the
224 East Pacific Ridge stand out. The eddy-permitting $1/12^\circ$ appears “noisy”. The pattern
225 of negative/positive values persist, and again this is locally quite confined. The ridge
226 structures are less clearly defined, and many more areas are seen to incur BPT responses.
227 Some features are also more pronounced, with the South-West Indian Ridge and Atlantic-
228 Indian Ridge standing out as extensions of the Scotia Ridge after the Drake Passage. The

²²⁹ BPT changes significantly with increased roughness from changing horizontal resolution,
²³⁰ moving away from clearly confined shelf features through a clearer influence of even deeper
²³¹ bathymetry and finally to a more stochastic but spatially connected picture.

232

²³³ The pattern of the BPT being similar but dispersed differently through increasing res-
²³⁴ olution is confirmed by the PDFs in the second row of Fig. 3. The latitudinally averaged
²³⁵ PDFs highlight that there appears to be a change in the kurtosis similar to the change in
²³⁶ roughness with increasing resolution. The scattered high values of the non-eddy resolving
²³⁷ 1° are spread throughout, while the higher resolutions have smoother PDFs. There is also
²³⁸ no apparent change with latitude, or significant increase visible in the Southern Ocean.
²³⁹ This suggests that the overall BPT term is similar in all three resolutions, when the ap-
²⁴⁰ propriate average is considered. The bottom row in Fig. 3 highlights this, as the globally
²⁴¹ averaged BPT PDF does not show a significant increase, and highlights the noisy nature
²⁴² of the non-eddy resolving 1° .

243

²⁴⁴ To elucidate the baroclinic component of the BPT term, the JEBAR term is shown in
²⁴⁵ Fig 4 for the 30 year mean. The JEBAR term is expected to be larger where we have
²⁴⁶ sharper gradients of H interacting with stratified flow. This type of interaction is found
²⁴⁷ specifically on the shelf break and in areas of sharp ∇H .

248

²⁴⁹ The top row of Fig. 4 illustrates geographically, that in the non-eddy resolving 1° most
²⁵⁰ of the activity is confined to the shelves for the 30 year mean JEBAR term. Compared
²⁵¹ to the BPT term there is less activity. The geographical distribution of the JEBAR

term in the intermediate resolution $1/4^\circ$ shows a pattern more similar to the BPT for the 30 year mean, where bathymetric features stand out but are less clearly partitioned with positive/negative features aligned with the mean flow. The eddy-permitting $1/12^\circ$ shows the JEBAR term being quite similar geographically to the BPT, appearing more “noisy” than the resolutions with less roughness; the bathymetric features stand out, but without the more coherent patterns of negative/positive BPT. Features such as the Pacific-Antarctic Ridge in the Pacific sector of the Southern Ocean are prominent, and the Scotia Ridge is clearly outlined in all resolutions, but we see that the influence of the region is increasingly visible with increasing resolution, e.g. in the eddy-permitting $1/12^\circ$ features like the mid-Atlantic Ridge are clear down to various fracture zones.

262

Certain regions have a negative/positive pattern, making it plausible that the effects of increasing resolution would average out with appropriate spatial averaging. The area averaged latitudinal PDFs in the second row of Fig. 4 demonstrates that this is not the case. The non-eddy resolving 1° , has a sharply peaked PDF throughout, with the distributions becoming increasingly spread out (lower kurtosis). This is a persistent feature, highlighted in the Southern Ocean where the eddy-permitting $1/12^\circ$ shows a very strongly skewed kurtosis. The global average PDF in the bottom row of Fig. 4 confirms this illustrating that the eddy-permitting $1/12^\circ$ is profoundly different from the non-eddy resolving 1° resolution, with the intermediate resolution $1/4^\circ$ somewhere in the middle. The changes in JEBAR highlight the barotropic component of the BPT compensation, that we expected from the baroclinic and barotropic components of the overturning streamfunction (Fig. 2). This is evident from the changes in the PDFs in Fig. 4, and we see that

²⁷⁵ this is particularly the case in regions such as the Southern Ocean where the mean flow
²⁷⁶ is expected to interact with rough bathymetry more than in the North Atlantic and Pacific.

²⁷⁷

²⁷⁸ The compensating nature of the BPT and JEBAR terms are highlighted for the lati-
²⁷⁹ tude 60°S in Fig. 5. The bottom panel shows the depth of the 1° (blue), 1/4° (black)
²⁸⁰ and 1/12° (red) for from non-eddy resolving, intermediate to eddy-permitting resolution
²⁸¹ respectively. The increased roughness is apparent, while the overall features remain the
²⁸² same. The top panel shows the BPT (orange) and JEBAR (light blue) terms for the asso-
²⁸³ ciated H for the non-eddy resolving 1°. There is only one area where there is considerable
²⁸⁴ activity, associated with the Drake passage. The JEBAR term is very small compared to
²⁸⁵ the BPT term. The second panel down illustrated the intermediate 1/4° resolution. This
²⁸⁶ shows more activity, with the BPT and JEBAR terms mirroring each other. The third
²⁸⁷ panel down shows the eddy-permitting 1/12° BPT and JEBAR terms for 60°S. There is
²⁸⁸ much more activity here, particularly associated with regions of rough bathymetry. Fig.
²⁸⁹ 5 illustrates that the JEBAR term makes up a significant proportion of the BPT. In the
²⁹⁰ interpretation of Fig. 5, the compensating nature of the JEBAR term as a complement to
²⁹¹ the BPT is apparent as e.g. positive BPT will often have negative JEBAR. The impor-
²⁹² tance of the degree of baroclinicity in the mean flow is seen in that the roughness alone
²⁹³ does not explain the degree of BPT/JEBAR interaction; the composition of the mean
²⁹⁴ flow is key.

²⁹⁵

4. Discussion and conclusion

Increasing the horizontal resolution of an ocean GCM increases the bathymetric roughness. The range of resolutions relevant to realistic ocean models deployed within climate simulations e.g. in support of the CMIP5 and CMIP6 efforts, starts at the non-eddy resolving 1° , and the eddy-permitting $1/12^\circ$ is still pushing the limits of modern computing and analysis capacity [Stouffer *et al.*, 2017, @; Eyring *et al.*, 2016, @]. The presented systematic assessment of the dynamic response of changing the roughness and allowing the mean flow to interact with the increased roughness is demonstrated to have a profound invigorating impact on Ψ . The root cause is found in the ability of to resolve eddies, as seen in the baroclinic component of Ψ whch is a prominent feature in the Southern Ocean. The change in roughness did not lead to a marked increase in the BPT term as a whole when appropriate area averaging is applied, but is clear in the baroclinic JEBAR component of the BPT term. The JEBAR term highlights the importance of the baroclinic eddy field interacting with rough bathymetry . Both the eddy field and the rough bathymetry are more prevalent in the Southern Ocean, where the largest changes both in Ψ and JEBAR are demonstrated.

The Southern Ocean is uniquely suited as a case study, as eddy processes are particularly important; H is critical due to a lack of western boundaries, and varying horizontal resolution allows a direct assessment of this effect. This is captured specifically by the BPT term. There is an increase in the interaction of the baroclinic component with topography (JEBAR) with increasing horizontal model resolution. This is consistent with the increase in overturning found for higher resolutions. Munk and Palmén, 1951 [@] were

318 one of the first to highlight the Southern Ocean as a unique place in the ocean, where no
 319 western boundary continents supply sufficient friction to balance the wind stress. This
 320 implies that the Southern Ocean is governed by another mechanism to balance forces.
 321 Munk and Palmén, 1951 [@[suggest that the wind stress is balanced by bottom friction
 322 where the ACC interacts with H, with the meridional components of the current making
 323 it span sufficient depth to allow this communication of stresses from surface to bottom.
 324 There is increased communication between the surface and deep ocean, as well as an in-
 325 creasing tendency towards barotropic columns (not shown) in the higher resolution. This
 326 suggests that the mechanism suggested by Munk and Palmén, 1951 [@[would be highly
 327 sensitive to changes in the horizontal resolution.

328

329 Penduff *et al.*, 2002 [@[illustrate that smoothing the H has a large effect on eddying
 330 flows, suggesting that changing ∇H could have large impacts. For all resolutions, the
 331 BPT term is similar for both the monthly mean field (not shown) and the 30 year mean.
 332 The effect of smoothing the bathymetry, but keeping the resolution the same in Penduff
 333 *et al.*, 2002 [@[confirms that the distribution of baroclinic work towards realising the
 334 overturning is sensitive to ∇H , rather than simply being reflected in the PBT term.

335

336 Wells and de Cuevas, 1995 [@[explore momentum balance in the Southern Ocean, ex-
 337 ploring the role of BPT but not the horizontal resolution. Here the wind stress term and
 338 the beta term are thought to dominate. They point out that the wind stress term is an
 339 order of magnitude smaller unless a zonal integral along streamlines is considered. This is
 340 because the sign of the wind remains constant, while other terms like the lateral friction

341 have varying sign. They show that the non-linear terms can be quite large, and the lateral
 342 friction is also seen to be non-negligible. A quasi-Sverdrupian regime is observed in the
 343 60-280°E Southern Ocean section (Approximately excluding the Atlantic Sector), where
 344 the ACC drifts South. This overlaps with regions where deep mixed layers are found.
 345 Assessing the longitudinal area averaged vorticity terms, the BPT is seen to balance beta.
 346 Diagnosing the main momentum sinks, Hughes and Killworth, 1995 [@] connect the main
 347 ACC momentum sinks with bathymetric features of the Patagonian shelf, the Campbell
 348 Plateau and the Pacific-Antarctic Ridge. These are revealed as the ACC drifts north,
 349 with the topographic features inducing a pressure difference. Wells and de Cuevas, 1995
 350 [...] demonstrate that the lateral friction can have a large impact, especially if the areas
 351 of the Drake passage and Scotia ridge are considered in a circumpolar average, suggesting
 352 that these areas are particularly important for dissipation of the wind input.

353

354 The steering effect of the BPT term can be seen in its interaction with H , with a vortex
 355 contraction (negative sign) as a flow hits an obstacle and a stretching (positive sign) as H
 356 deepens after the obstacle. The BPT term does not change greatly with resolution. How-
 357 ever, large changes are seen in the partitioning of the baroclinic and barotropic (JEBAR)
 358 contributions to the term. The JEBAR term changes greatly with resolution, partic-
 359 larly in the Southern Ocean. This is likely the main source of the enhanced baroclinic
 360 anti-clockwise circulation in the Southern Ocean. The increased importance of JEBAR
 361 suggests that as the resolution increases the meridional flow is increasingly pushed to-
 362 wards the case where $f \frac{\Delta H}{H} \gg \beta$ is more important than following f-contours. The direct
 363 implication for modeling efforts concerns the sensitivity to parameterization of interac-

³⁶⁴ tions with bathymetry. Increasing JEBAR suggests that decisions regarding e.g. no-slip
³⁶⁵ or free-slip can increasingly impact the direction of currents. Hughes and de Cuevas, 2001
³⁶⁶ [@] noted that BPT can in the free-slip case be interpreted as a simply “up-hill” flow,
³⁶⁷ while with no-slip it would be a viscous stress divergence at the bottom. This idea of
³⁶⁸ “roughness” being critical is explored by Schoonover *et al.*, 2017 [@], suggesting that the
³⁶⁹ key aspect for WBC separation is the transition of the BPT from mainly barotropic to
³⁷⁰ more baroclinic.

371

³⁷² The link between the overturning and the PBT term is explored by Yeager, 2015 [@],
³⁷³ highlighting the importance of the BPT term in the closure of the gyre and overturning
³⁷⁴ circulation in the North Atlantic was highlighted. Yeager, 2015 [@] used 15 year inte-
³⁷⁵ grations of a 1° and a $1/10^\circ$ version of the POP2 model with 62 vertical levels. The
³⁷⁶ study illustrates that the BPT term is dominant in the vorticity balance of the Atlantic
³⁷⁷ meridional overturning circulation, representing a key link between the gyre and over-
³⁷⁸ turning circulation. The BPT term is found to act as the coupling between the large scale
³⁷⁹ barotropic and baroclinic flows. The present work illustrates that these conjectures can be
³⁸⁰ applied globally, and that the Southern Ocean is particularly sensitive to this topographic
³⁸¹ coupling through the baroclinic component of the BPT term. The connection between
³⁸² the overturning and the BPT/JEBAR term explored by Yeager, 2015 [@] are describe
³⁸³ “momentum dominated” (BPT), and “buoyancy dominated” (JEBAR) areas. The later
³⁸⁴ are connected to the overturning, and assessed using the JEBAR term. The use of JEBAR
³⁸⁵ can be problematic under certain conditions as discussed in the appendix.

386

387 The BPT term in non-dissipative, impacting the location of dissipation. Nikurashin *et*
 388 *al.*, 2013 [@] discuss ways energy is dissipated in geostrophic flows, also highlighting the
 389 importance of the Southern Ocean as the primary location of wind power input, where
 390 the westerly winds are aligned with the ACC. This creates a store of potential energy,
 391 which is released through baroclinic instabilities in a vigorous geostrophic eddy field. The
 392 location of this release is sensitive to ∇H , as well as what work is done through its re-
 393 lease. LaCase and Isachsen, 2010 [@] summarizes the conventional understanding that
 394 eddies provide the mechanism for meridional transport in the ACC, supported by results
 395 presented here. The Southern Ocean acts like a channel flow. The BPT acts to transfer
 396 barotropic vorticity from the neighbouring gyres into the zonal jet, as well as returning
 397 the wind-driven flows along the western boundaries of the partial topographic barriers.
 398 The depth-integrated flow, steered by H , controls where the bottom friction dissipates the
 399 potential vorticity. Throughout the Southern Ocean, different potential vorticity states can
 400 be attained in separate sub-basins. Increasing the resolution, the JEBAR term highlights
 401 where the change in contribution to Ψ is taking place.

402

403 In summary, the change in the partitioning of the baroclinic (JEBAR) and barotropic
 404 part of the BPT illustrates an increase in the importance of the baroclinic topographic
 405 interactions with resolution. Our results suggest that this is what gives rise to the in-
 406 creased baroclinic contribution to the overturning, seen in the 30 year mean overturning.
 407 This has implications for the balance of forces, suggesting that significant changes can
 408 take place when the resolution increases. The changes with resolution of interactions with

⁴⁰⁹ H in terms of vortex stretching was found mainly in the baroclinic JEBAR component.

⁴¹⁰

Appendix A: An intuition for BPT

⁴¹¹ Moving from the barotropic momentum equation to the barotropic vorticity equation

⁴¹² is demonstrated by Hughes and de Cuevas, 2001 [@]; Yeager, 2015 [@]; Schoonover *et al.*,

⁴¹³ 2016 [@]. Due to the BPT term's sensitivity to topographic roughness, it is worth devel-

⁴¹⁴ oping a physical intuition for the interpretation of the term. Under a geostrophic scaling,

⁴¹⁵ the BPT can be interpreted as vortex tube stretching. Following Cane *et al.*, 1998 [@],

⁴¹⁶ forming a vorticity equation and then vertically integrating:

⁴¹⁷

$$\beta\psi_x = -fw_b + \mathbf{k} \cdot \nabla \times \frac{\tau_w}{\rho_0} + R. \quad (\text{A1})$$

⁴¹⁸ The transport streamfunction ψ is the depth integrated stream function, and w_b is the

⁴¹⁹ vertical component velocity at the ocean floor:

⁴²⁰

$$w_b = u_b \cdot \nabla(H) = \frac{1}{\rho_0 f} J(p, H)|_b. \quad (\text{A2})$$

⁴²¹ The subscript b indicates the term is evaluated at the bottom, and u_b is the horizontal

⁴²² *geostrophic* velocity at the sea floor, and the final relation is a consequence of geostrophy.

⁴²³ J is the Jacobian defined as: $J(u, v) = u_x v_y - u_y v_x$.

⁴²⁴ Note that mathematically, the $J(p, H)|_b$ is equivalent to the more familiar $J(p_b, H)$

⁴²⁵ according to:

$$J(p_b, H) = \frac{\partial p_b}{\partial x} \frac{\partial H}{\partial y} - \frac{\partial p_b}{\partial y} \frac{\partial H}{\partial x} = J(p, H)_b, \quad (\text{A3})$$

⁴²⁶ where p_b is the pressure evaluated at the bottom ($z = -H$), since:

$$\begin{aligned} \frac{\partial p_b}{\partial x} &= \left. \frac{\partial p}{\partial x} \right|_z + \left. \frac{\partial p}{\partial z} \right|_x z \\ &= \left. \frac{\partial p}{\partial x} \right|_z + \rho g \frac{\partial H}{\partial x}, \end{aligned} \quad (\text{A4})$$

⁴²⁷ and the equivalent term for $\frac{\partial p_b}{\partial y}$ cancel out.

428

⁴²⁹ Increasingly resolving small scale features of rough bathymetry (∇H), Cane *et al.*, 1998
⁴³⁰ [@]; Yeager, 2015 [@] discuss how a uniform density ocean will have its inviscid flow con-
⁴³¹ strained following geostrophic f/H contours [Pedlowski, 1979, @]. Barotropic flow will
⁴³² cross f/H contours to balance the vorticity input by the winds, implying an imprint on the
⁴³³ overturning characteristics with changing model resolution. For a flat bottom, we would
⁴³⁴ look at f contours. However, in NEMO, the realistic bathymetry offers very interesting H
⁴³⁵ contours. These gradients in H imply interesting deep flow, and convergence/divergence
⁴³⁶ in regions relative to pure β -effect regions. In this sense, we arrive at Eq. A2.

437

⁴³⁸ The theoretical link between the relief, bottom velocity and vortex stretching, motivates
⁴³⁹ an assessment of BPT and its baroclinic component; the Joint Effect of Baroclinicity and
⁴⁴⁰ Relief (JEBAR). The BPT arises in the vorticity equation of vertically integrated horizon-
⁴⁴¹ tal velocity, while the Joint Effect of Baroclinicity and Relief (JEBAR) term arises from
⁴⁴² the vertically-averaged horizontal velocity [Yeager, 2015, @; Bell, 1999, @; Greatbatch *et*
⁴⁴³ *al.*, 1991, @; Mertz and Wright, 1992, @]. In this manner, JEBAR represents the BPT

⁴⁴⁴ component that is associated with the buoyancy dependent and baroclinic part of the
⁴⁴⁵ pressure gradient, vanishing in the absence of stratification.

446

⁴⁴⁷ Expressing the BPT in terms of the barotropic depth averaged flow:

$$\frac{1}{\rho_0} J(p_b, H) = f \mathbf{u}_{gb} \cdot \nabla H = \overbrace{f(\mathbf{u}_{gb} - \bar{\mathbf{u}}_g) \cdot \nabla H}^{\text{Baroclinic}} + \overbrace{f \bar{\mathbf{u}}_g \cdot \nabla H}^{\text{Barotropic}}. \quad (\text{A5})$$

⁴⁴⁸ Mertz and Wright, 1992 [@] highlight that the expression for BPT is the sum of a baroclinic
⁴⁴⁹ (JEBAR) and barotropic component. Appendix B details moving from the geostrophic
⁴⁵⁰ balance in the meridional momentum equation to find the JEBAR term as $\frac{1}{H} J(\Phi, H)$,
⁴⁵¹ where Φ is the potential energy per unit area: $\Phi = \frac{g}{\rho_0} \int_{-H}^0 z \rho dz$.

452

⁴⁵³ Substituting A5 into the vorticity Eq. A1, and introducing Ψ , we find that:

$$\beta \frac{\partial \Psi}{\partial x} = \frac{1}{H} J(\Phi, H) + f \bar{\mathbf{u}}_g \cdot \nabla H + \frac{1}{\rho_0} [\mathbf{k} \cdot \nabla \times \boldsymbol{\tau}]. \quad (\text{A6})$$

⁴⁵⁴ Then:

$$H \bar{\mathbf{u}}_g + \frac{\mathbf{k} \times \boldsymbol{\tau}}{\rho_0 f} = H \bar{\mathbf{u}}_{total}. \quad (\text{A7})$$

⁴⁵⁵ It follows that:

$$\begin{aligned} \beta \frac{\partial \Psi}{\partial x} &= \frac{1}{H} J(\Phi, H) + \frac{f}{H} J(\Psi, H) + H \rho_0^{-1} \mathbf{k} (\nabla \times \frac{\boldsymbol{\tau}}{H}), \\ \Rightarrow \frac{1}{H} J(\Psi, f) - \frac{f}{H^2} J(\Psi, H) &= \frac{1}{H^2} J(\Phi, H) + \rho_0^{-1} (\mathbf{k} \cdot \nabla \times \frac{\boldsymbol{\tau}}{H}), \\ \Rightarrow \frac{1}{H} J \left(\Psi, \frac{f}{H} \right) &= -J \left(\Psi, \frac{1}{H} \right) + \rho_0^{-1} (\mathbf{k} \cdot \nabla \times \frac{\boldsymbol{\tau}}{H}). \end{aligned} \quad (\text{A8})$$

⁴⁵⁶ Here the term $J(\Phi, \frac{1}{H})$ is the JEBAR term [Mertz and Wright, 1992, @; Sarkisyan and
⁴⁵⁷ Ivanov, 1971, @].

458

⁴⁵⁹ There are several interpretations of this in the context of real ocean flows. Myers *et*
⁴⁶⁰ *al.*, 1996 [@] suggests that it illustrates the difference between bottom pressure torque
⁴⁶¹ and the corresponding torque associated with depth averaged pressure, while Mertz and
⁴⁶² Wright, 1992 [@] also suggest it relates to bottom torque (as the curl of the horizontal
⁴⁶³ force by the bottom of the fluid) but also that it can be seen as the geostrophic component
⁴⁶⁴ of the correction to the topographic stretching term. This accounts for that it is in fact
⁴⁶⁵ the bottom velocity, not the depth averaged velocity, which gives rise to the vortex-tube
⁴⁶⁶ stretching.

467

Appendix B: JEBAR derivation

⁴⁶⁸ Expressing JEBAR $f(\mathbf{u}_{gb} - \bar{\mathbf{u}}_g) \cdot \nabla H$ in terms of the baroclinic structure, the geostrophic
⁴⁶⁹ balance in the meridional momentum equation is used:

$$-f\mathbf{u} = -\frac{p_x}{\rho_0}, \quad (\text{B1})$$

$$\Rightarrow -f\bar{\mathbf{u}} = -\frac{1}{H} \int_{-H}^0 \frac{p_x}{\rho_0} dz. \quad (\text{B2})$$

⁴⁷⁰ Here B2 is the vertical average (denoted by the overbar) of the geostrophic balance in B1.
⁴⁷¹ Now we use the hydrostatic approximation:

$$p = p_b - \int_{-H}^z g\rho dz', \quad (\text{B3})$$

$$\Rightarrow -f\bar{\mathbf{u}} = -\frac{1}{\rho_0}p_{bx} + \frac{1}{\rho_0 H} \frac{\partial}{\partial x} \int_{-H}^0 \int_{-H}^z g\rho dz' dz, \quad (\text{B4})$$

integration by parts gives us:

$$-f\bar{u} = -\frac{1}{\rho_0}p_{bx} + \frac{1}{\rho_0 H} \frac{\partial}{\partial x} \left[- \int_{-H}^0 z g\rho dz' + \left[z \int_H^z g\rho dz' \right]_{-H}^0 \right], \quad (\text{B5})$$

⁴⁷² which we re-write as:

$$-f\bar{\mathbf{u}} = -f\mathbf{u}_b - \frac{1}{H}\Phi_x, \quad (\text{B6})$$

$$\Phi = \frac{g}{\rho_0} \int_{-H}^0 z \rho dz. \quad (\text{B7})$$

⁴⁷³ Where Φ is the potential energy per unit area.

we find the JEBAR term:

$$f(\mathbf{u}_{gb} - \bar{\mathbf{u}}_g) \cdot \nabla H = \frac{1}{H}J(\Phi, H), \quad (\text{B8})$$

⁴⁷⁴ and so:

$$\frac{1}{\rho_0}J(p, H)_b = \frac{1}{H}J(\Phi, H) + f\bar{\mathbf{u}}_g \cdot \nabla H. \quad (\text{B9})$$

Appendix C: Use and disuse of JEBAR

⁴⁷⁵ To critically examine the use of the JEBAR term, four cases are interesting:

⁴⁷⁶ 1. Flat seabed: $J(p_b, H) = 0$

477 2. Barotropic flow: $\bar{\mathbf{u}}_g$ dominates, and $f(\mathbf{u}_{gb} - \bar{\mathbf{u}}_g) \cdot \nabla H \ll f\bar{\mathbf{u}}_g \cdot \nabla H$
 478 3. Surface flow $\bar{\mathbf{u}}_s$ is large compared to \mathbf{u}_gb . This creates spurious values and makes
 479 calculations unreliable.

480 4. The bottom geostrophic flow \mathbf{u}_{gb} is sizable compared to the surface flow $\bar{\mathbf{u}}_s$. **This**
 481 **is the interesting space in which JEBAR can give valuable insight.**

482 Cases 1 and 2 are not likely to be important in the ocean. Case 4. is the interesting
 483 one, which covers most of the ocean in our paper. Case 3 is the one Cane *et al.*, 1998
 484 [@] pointed to as problematic, but is not seen in the 30 year mean fields. Developing a
 485 threshold of the ratio of $\bar{\mathbf{u}}_s \gg \mathbf{u}_{gb}$ which renders JEBAR unusable is outside the scope of
 486 this paper, but should be determined before JEBAR can be useful to guide observational
 487 work where this case may be relevant.

488

Appendix D: Extended BPT-JEBAR compensation example

489 Fig. 6 shows a detail of Fig. 5.

Appendix E: Figures

References

- 490 Arakawa, A. and Lamb, V.R.: Computational design of the basic dynamical process of
 491 the UCLA general circulation model, Methods in Computational Physics, 17, Academic
 492 Press, New York, 173-265, 1977.
 493 Barnier, B., Madec, G., Penduff, T., Molines, J.M., Treguier, A.M., Le Sommer, J.,
 494 Beckmann, A., Biastoch, A., Bning, C., Dengg, J., Derval, C., Durand, E., Gulev, S.,

- 495 Remy, E., Talandier, C., Theetten, S., Maltrud, M., McClean, J., and De Cuevas, B.:
 496 Impact of partial steps and momentum advection schemes in a global ocean circulation
 497 model at eddy permitting resolution, *Ocean Dynam.*, 56, 543-567, doi:10.1007/s10236-
 498 006-0082-1, 2006.
- 499 Bell, M.J.: Vortex stretching and bottom torques in the Bryan-Cox ocean circulation
 500 model, *J. Geophys. Res.*, 104, 23545-23563, 1999.
- 501 Bourdallé-Badie, R., Treguier, A.M., Molines, J.M., Coward, A., Scheinert, M., Lu, Y.,
 502 Lecointre, A. and Tranchant, B.: The ORCA12 bathymetry V3.2. Technical report,
 503 MERCATOR-DRAKKAR report, 2012.
- 504 Brodeau, L., Barnier, B., Treguier, A.M., Penduff, T. and Gulev, S.: An ERA40-based
 505 atmospheric forcing for global ocean circulation models, *Ocean Modelling*, 31 (3-4),
 506 88-104, 2010.
- 507 fire Cane, M.A., Kamenkovich, V.M. and Krupitsky, A.: On the Utility and Disutility of
 508 JEBAR, *J. Phys. Oceanogr.*, 28, 519-526. doi: 10.11751520-0485(1998)028, 1998.
- 509 Coward, A. C.: The ORCA1 model bathymetry, <http://www.noc.soton.ac.uk/nemo/?page=bathyimages>, National Oceanography Centre, Southampton, UK, 2006.
- 510 Dewar, R.C., Lineweaver, C.H., Niven, R.K. and Regenauer-Lieb, K. (eds.), Beyond
 511 the Second Law, Understanding Complex Systems, DOI: 10.1007/978-3-642-40154-1_1,
 512 Springer-Verlag Berlin Heidelberg, 2014.
- 513 Eyring, V., Bony, S., Meehl, G. A., Senior, C. A., Stevens, B., Stouffer, R. J., and Taylor, K. E.: Overview of the Coupled
 514 Model Intercomparison Project Phase 6 (CMIP6) experimental design and organization, *Geosci. Model Dev.*, 9, 1937-
 515 1958, doi:10.5194/gmd-9-1937-2016, 2016.

- 517 Döös, K., and Webb, D.J.: The Deacon cell and the other meridional cells of the Southern
 518 Ocean, *J. Phys. Oceanogr.*, 24(2), 429-442, 1994.
- 519 Greatbatch, R.J., Fanning, A.F., Goulding, A.D. and Levitus, S.: A diagnosis of interpen-
 520 tadal circulation changes in the North Atlantic, *J. Geophys. Res.*, 96 (C12), 22 009-22
 521 023, 1991.
- 522 Griffies, S.M., Pacanowski, R.C. and Hallberg, R.W.: Spurious diapycnal mixing asso-
 523 ciated with advection in a z-coordinate ocean model, *Mon. Wea. Rev.*, 128, 538-564,
 524 2000.
- 525 Hewitt, H.T., Copsey, D., Culverwell, I.D., Harris, C.M., Hill, R.S.R., Keen, A.B.,
 526 McLaren, A.J. and Hunke E.C.: Design and implementation of the infrastructure of
 527 HadGEM3: the next-generation Met Office climate modelling system, *Geosci. Model
 Dev.*, 4 (2), 223-253, doi:10.5194/gmd-4-223-2011, 2011.
- 528 Hughes, C.W. and Killworth, P.D.: Effects of Bottom Topography in the Large-Scale
 529 Circulation of the Southern Ocean, *J. Phys. Oceanogr.*, 25, 2485-2497, doi: [http://dx.doi.org/10.1175/1520-0485\(1995\)025<2485:EOTIT>2.0.CO;2](http://dx.doi.org/10.1175/1520-0485(1995)025<2485:EOTIT>2.0.CO;2), 1995.
- 530 Hughes, C.W. and de Cuevas, B.A.: Why western boundary currents in realistic
 531 oceans are inviscid: a link between form stress and bottom pressure torques, *Jour-
 532 nal of Physical Oceanography*, 31 (10), 2871-2885. doi: [http://dx.doi.org/10.1175/1520-0485\(2001\)031<2871:WWBCIR>2.0.CO;2](http://dx.doi.org/10.1175/1520-0485(2001)031<2871:WWBCIR>2.0.CO;2), 2001.
- 533 IPCC: Climate Change 2013: The Physical Science Basis. Contribution of Working Group
 534 I to the Fifth Assessment Report of the Intergovernmental Panel on Climate Change
 535 [Stocker, T.F., D. Qin, G.K. Plattner, M. Tignor, S.K. Allen, J. Boschung, A. Nauels, Y.
 536 Xia, V. Bex and P.M. Midgley (eds.)]. Cambridge University Press, Cambridge, United

540 Kingdom and New York, NY, USA, 1535 pp, doi:10.1017/CBO9781107415324, 2013.

541 LaCasce, J.H. and Isachsen, P.E. (2010). The linear models of the ACC. Progress in

542 Oceanography. ISSN 0079-6611. 84(3-4), s 139- 157 . doi:10.1016/j.pocean.2009.

543 11.002

544 Jackett, D.R. and McDougall, T.J.: Minimal adjustment of hydrographic data to achieve

545 static stability, J. Atmos. Ocean Tech., 12, 381-389, 1995.

546 Jackson, L., Hughes, C.W. and Williams, R.G.: Topographic Control of Basin and Chan-

547 nel Flows: The Role of Bottom Pressure Torques and Friction, J. Phys. Oceanogr., 36,

548 1786-1805. doi: <http://dx.doi.org/10.1175/JPO2936.1>, 2006.

549 Lee, MM., Coward, A.C., and Nurser, A.J.G.: Spurious diapycnal mixing of the deep

550 waters in an eddy-permitting global ocean model, Journal of Physical Oceanography,

551 32 (5), 1522-1535. 10.1175/1520-0485(2002)032j1522:SDMOTD;2.0.CO;2, 2002.

552 Luyten

553 Madec, G.: NEMO ocean engine, Note du Pole de modlisation, Institut Pierre-Simon

554 Laplace (IPSL), 27, 2008.

555 Marsh, R., de Cuevas, B.A., Coward, A.C., Jacquin, J., Hirschi, J.J.M., Aksenov, Y.,

556 Nurser, A.J.G. and Josey, S.A.: Recent changes in the North Atlantic circulation sim-

557 ulated with eddy-permitting and eddy-resolving ocean models, Ocean Modelling 28(4),

558 226-239, url: <http://dx.doi.org/10.1016/j.ocemod.2009.02.007>, 2009.

559 Marzocchi, A., Hirschi, J.J.M., Penny, H.N., Cunningham, S.A., Blaker, A.T. and Coward,

560 A.C.: The North Atlantic subpolar circulation in an eddy-resolving global ocean model,

561 Journal of Marine Systems, 142, doi:126-143. 10.1016/j.jmarsys.2014.10.007, 2015.

- 562 Megann, A.P., Storkey, D., Aksenov, Y., Alderson, S., Calvert, D., Graham, T., Hyder,
 563 P., Siddorn, J. and Sinha, B.: GO 5.0: The joint NERC-Met Office NEMO global ocean
 564 model for use in coupled and forced applications, Geotechnical Model Development, 7
 565 (3), 1069-1092, doi:10.5194/gmd-7-1069-2014, 2014.
- 566 Mertz, G. and Wright, D.G.: Interpretations of the JEBAR Term, J. Phys. Oceanogr., 22,
 567 301-305, doi: [http://dx.doi.org/10.1175/1520-0485\(1992\)022<0301:IOTJT>2.0.](http://dx.doi.org/10.1175/1520-0485(1992)022<0301:IOTJT>2.0.)
 568 CO;2, 1992.
- 569 Munk, W., 1950: On the wind-driven ocean circulation. J. Meteor., 7, 7993,
 570 doi:10.1175/1520-0469(1950)007j0080:OTWDOC;2.0.CO;2.
- 571 Munk, W.H., and Palmén, E,: Note on the dynamics of the Antarctic Circumpolar Cur-
 572 rent, Tellus, 3, 53-55, 1940.
- 573 Myers, P.G., Fanning, A.F. and Weaver, A.J.: JE BAR, Bottom Pressure Torque, and
 574 Gulf Stream Separation, J. Phys. Oceanogr., 26, 671-683, doi: [http://dx.doi.org/10.1175/1520-0485\(1996\)026<0671:JBPTAG>2.0.CO;2](http://dx.doi.org/10.1175/1520-0485(1996)026<0671:JBPTAG>2.0.CO;2), 1996.
- 575 Naveira Garabato, A.C., Nurser, A.J.G., Scott, R.B. and Goff, J.A.: The Impact of
 576 Small-Scale Topography on the Dynamical Balance of the Ocean, J. Phys. Oceanogr.,
 577 43, 647-668. doi: <http://dx.doi.org/10.1175/JPO-D-12-056.1>, 2013.
- 578 Nikurashin, M., Vallis, G.K. and Adcroft, A.: Routes to Energy Dissipation for
 579 Geostrophic Flows in the Southern Ocean, Nature Geosci 6, 1, 48-51, 2013.
- 580 Nurser, G.A. and Lee, M.M.: Isopycnal Averaging at Constant Height. Part II: Relating
 581 to the Residual Streamfunction in Eulerian Space, J. Phys. Oceanogr., 34, 2740-2755,
 582 doi: <http://dx.doi.org/10.1175/JPO2650.1>, 2004.
- 583 Pedlowski, J.: Geophysical Fluid Dynamics, Springer, 1979.

- 585 Penduff, T., Barnier, B., Verron, J., Kerbiriou, M.A.: How topographic smoothing contributes to differentiating the eddy flows simulated by sigma- and z-level models, J.
 586 Phys. Oceanogr., 32, 122-137, 2002.
- 588 Sarkisyan, A.S., and Ivanov, V.F.: The combined effect of baroclinicity and bottom relief
 589 as an important factor in the dynamics of ocean current, Izv. Acad. Sci. USSR Atmos.
 590 Oceanic Phys., Engl. Transl., 1, 173-188, 1971.
- 591 Scaife, A. A., Copsey, D., Gordon, C., Harris, C., Hinton, T., Keeley, S., ONeill, A.,
 592 Roberts, M., and Williams, K.: Improved Atlantic winter blocking in a climate model,
 593 Geophys. Res. Lett., 38, L23703, doi:10.1029/2011GL049573, 2011.
- 594 Schoonover, J., Dewar, W., Wienders, N., Gula, J., McWilliams, J.C., Molemaker, M.J.,
 595 Bates, S.C., Danabasoglu, G. and Yeager, S.: North Atlantic Barotropic Vorticity Bal-
 596 ances in Numerical Models, Journal of Physical Oceanography 2016 46:1, 289-303
- 597 Schoonover, J., W.K. Dewar, N. Wienders, and B. Deremble, 2017: Local
 598 Sensitivities of the Gulf Stream Separation. J. Phys. Oceanogr., 47, 353373,
 599 <https://doi.org/10.1175/JPO-D-16-0195.1>
- 600 Stouffer, R.J., V. Eyring, G.A. Meehl, S. Bony, C. Senior, B. Stevens, and K.E. Taylor, 2017: CMIP5 Scientific Gaps and
 601 Recommendations for CMIP6. Bull. Amer. Meteor. Soc., 98, 95105, <https://doi.org/10.1175/BAMS-D-15-00013.1>
- 602 Stommel, H. (1948), The westward intensification of wind-driven ocean currents, Eos
 603 Trans. AGU, 29(2), 202206, doi:10.1029/TR029i002p00202.
- 604 Stommel, H., and Arons, A.B.: On the abyssal circulation of the world ocean. Part I:
 605 Stationary planetary patterns on a sphere. Deep-Sea Res., 6, 140-154, 1960a.
- 606 Stommel, H. and Arons, A.B.: On the abyssal circulation of the world ocean. Part II: An
 607 idealized model of the circulation pattern and amplitude in oceanic basins. Deep-Sea

- 608 Res., 6, 217-233, 1960b.
- 609 Sverdrup, H.: Wind-driven currents in a baroclinic ocean; with application to the equatorial
610 currents of the eastern Pacific, Proc. Natl. Acad. Sci. (USA), 33, 318-326, 1947.
- 611 Thomas, L.N.: Formation of intrathermocline eddies at ocean fronts by wind-driven de-
612 struction of potential vorticity, Dynam. Atmos. Oceans, 45, 252-273, 2008.
- 613 Thomas, M.D., De Boer, A.M., Johnson, H.L. and Stevens, D.P.: Spatial and Temporal
614 Scales of Sverdrup Balance, J. Phys. Oceanogr., 44, 2644-2660. doi: <http://dx.doi.org/10.1175/JPO-D-13-0192.1>, 2014.
- 615 Wells, N.C. and De Cuevas, B.A.: Depth-Integrated Vorticity Budget of the Southern
616 Ocean from a General Circulation Model, J. Phys. Oceanogr., 25, 2569-2582. doi: [http://dx.doi.org/10.1175/1520-0485\(1995\)025<2569:DIVBOT>2.0.CO;2](http://dx.doi.org/10.1175/1520-0485(1995)025<2569:DIVBOT>2.0.CO;2), 1995.
- 617 Wunsch, C.: The decadal mean ocean circulation and Sverdrup balance, J. Mar. Res. 69,
618 417-434, 2011.
- 619 Yeager, S.: Topographic coupling of the Atlantic overturning and gyre circulations, J.
620 Phys. Oceanogr., 45, 1258-1284. doi: <http://dx.doi.org/10.1175/JPO-D-14-0100.1>,
621 2015.
- 622 Zika, J.D., England, M.H. and Sijp, W.P.: The Ocean Circulation in Thermohaline Co-
623 ordinates, Journal of Physical Oceanography, 2, 708-724, 2012.

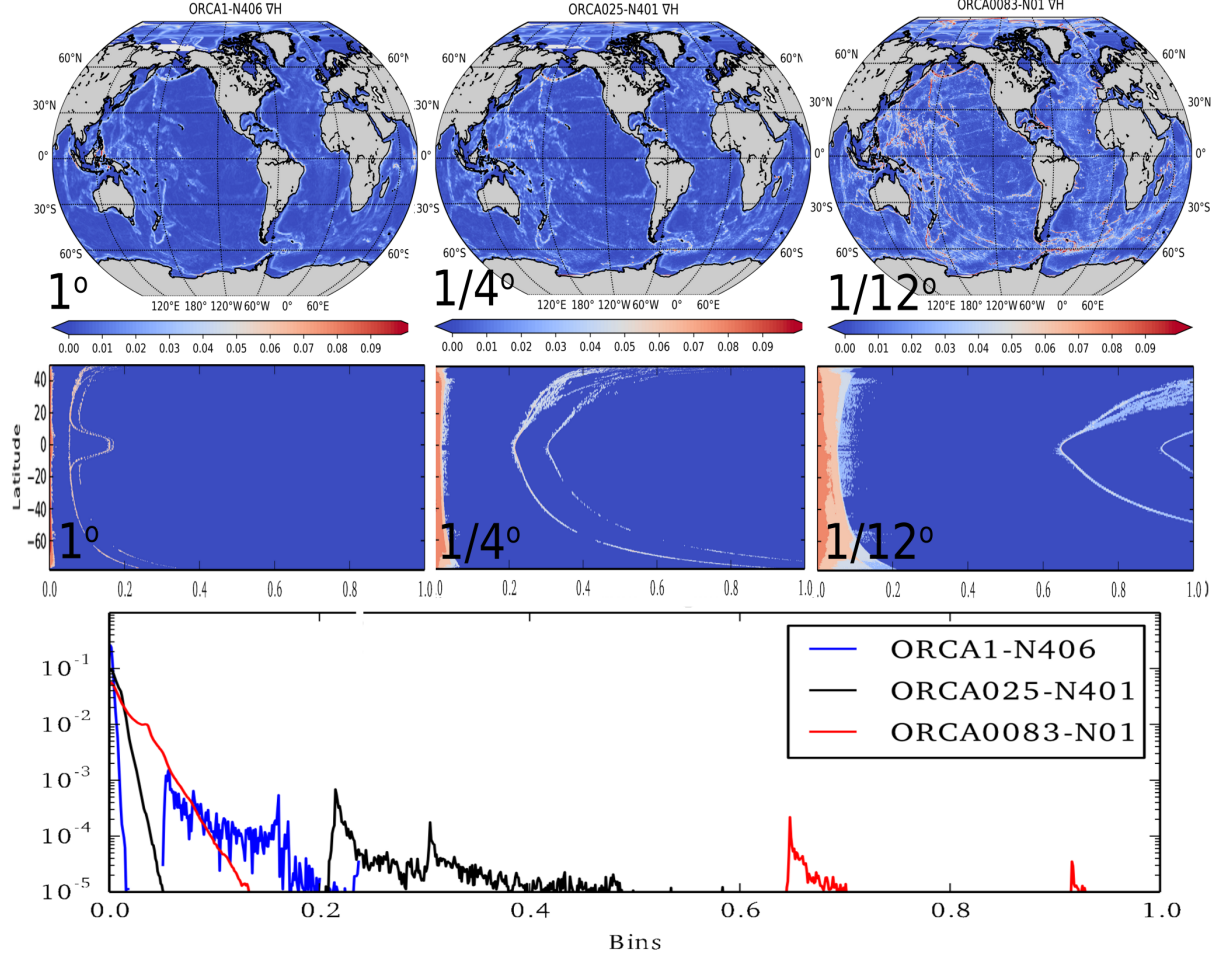


Figure 1. The roughness of the bathymetry changes drastically with resolution.

Top row shows the geographic locations of the roughness of the 1° (left column), $1/4^\circ$ (middle column) and $1/12^\circ$ (right column) for from non-eddy resolving, intermediate to eddy-permitting. The middle row illustrates the same as zonal area-averaged PDFs of each latitude. These illustrate the increase in roughness as the distributions become wider with increasing resolution. The bottom plot shows the global area averaged PDF, demonstrating the overall increase in roughness and the discingly different nature of the roughness that the resolutions allow. The “stripes” in the PDFs are proportional to the resolution, and highlight the tropical mesh refinement nesssesairy at 1° .

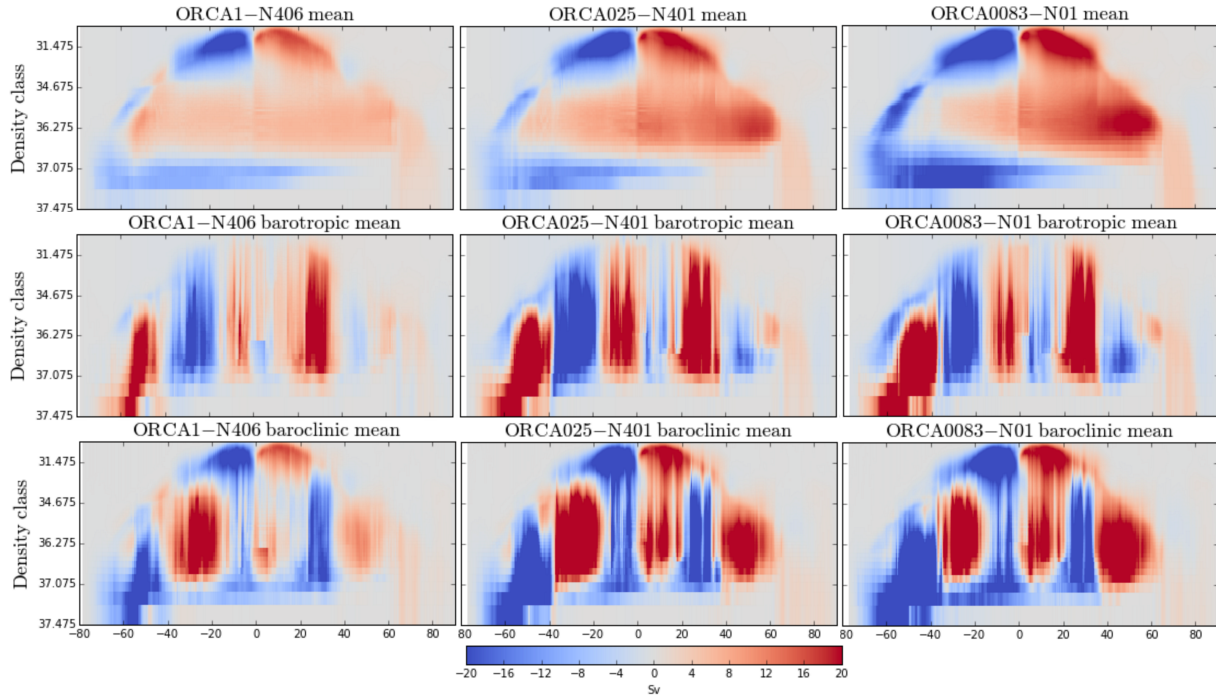


Figure 2. The gloabl zonally integrated ψ of the 30 year time mean for the full (top row), barotropic (middle row) and baroclinic (bottom row) global ocean. Three resolutions of 1° (left column), $1/4^\circ$ (middle column) and $1/12^\circ$ (right column) for from non-eddy resolving, intermediate to eddy-permitting. The clockwise (red) and anti-clockwise (blue) circulation is seen to change significantly with resolution, with the anti-clockwise circulation in the Southern Hemisphere standing out. The baroclinic and barotropic components largely compensate for each other, with significant changes being found in the strengthening of the baroclinic component with increasin resolution. This is attributed to increasingly being able to resolve the scales relevant to eddies, and suggestive of eddy compensation.

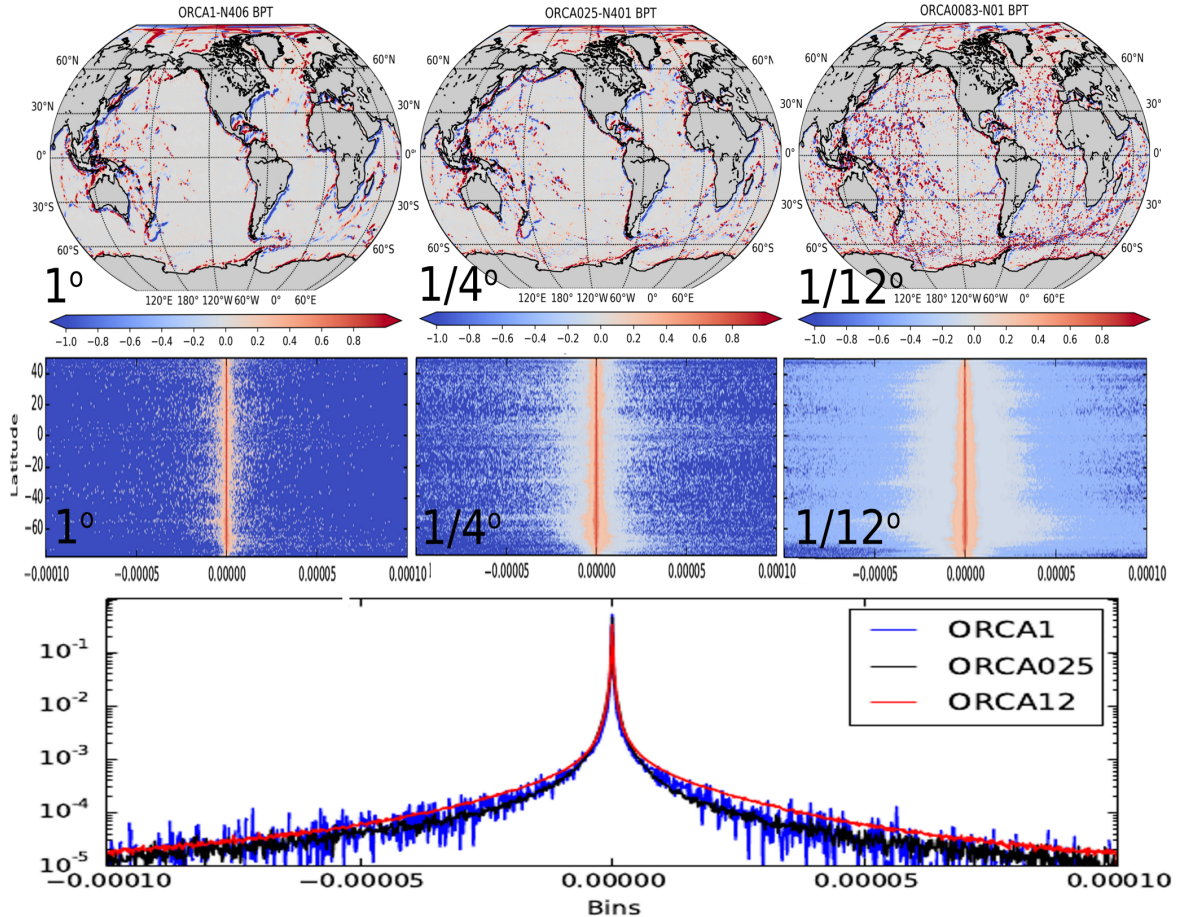


Figure 3. The change in BPT is not confined to the Southern Ocean. Top row shows the geographic locations of the BPT of the 1° (left column), $1/4^\circ$ (middle column) and $1/12^\circ$ (right column) for from non-eddy resolving, intermediate to eddy-permitting. The smooth initial nature of negative (blue) BPT downstream of an obstacle and positive (red) upstream becomes increasingly obscured as the roughness increases with resolution. The middle row illustrates the same as zonal area-averaged PDFs of each latitude. A decrease in kurtosis (how “peaked” the PDF is) is seen increasing the resolution, meaning the BPT is not confined to geographically limited areas but found more generally. The Southern Ocean is not seen to stand out. The bottom globally averaged PDF illustrates that this feature is noteable, but may not differ significantly globally speaking.

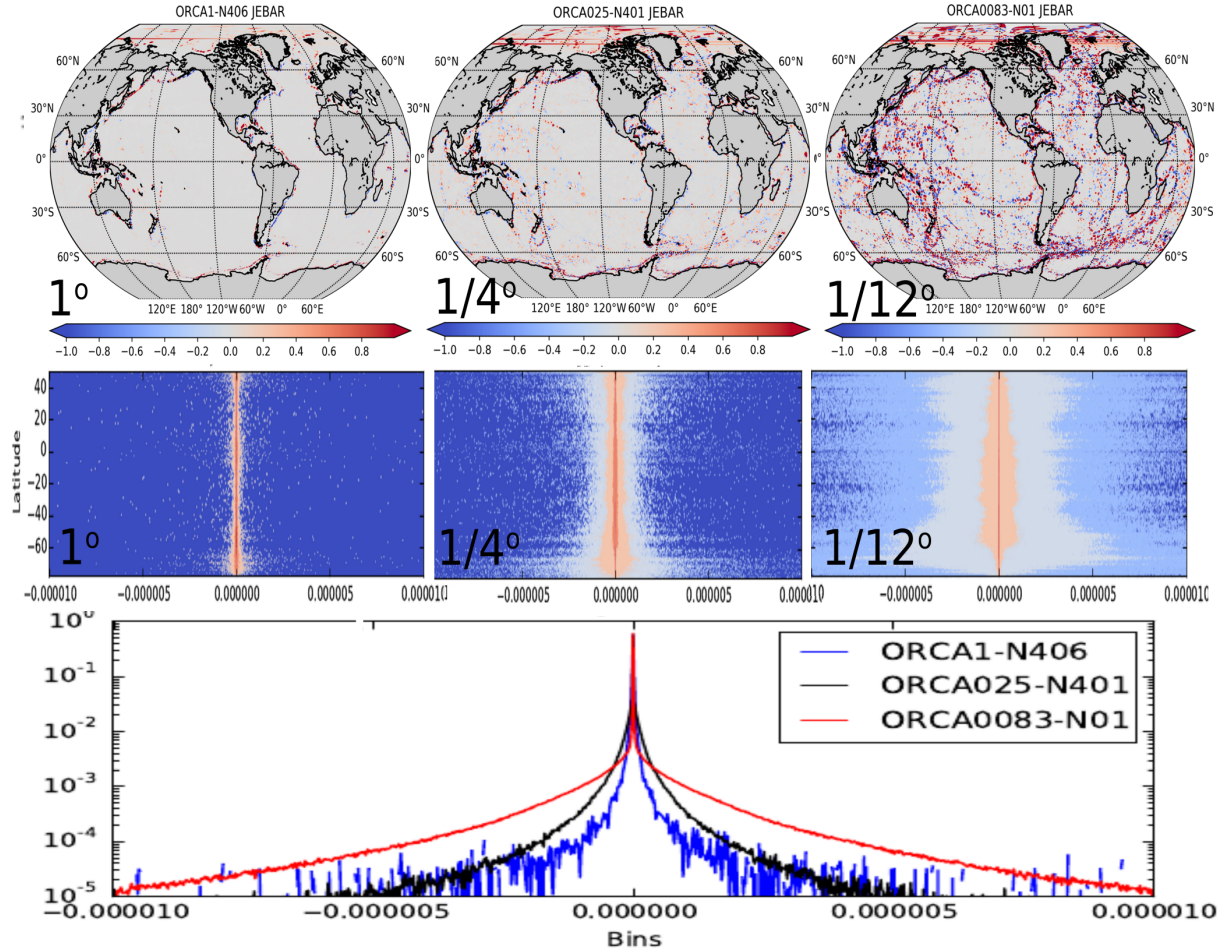


Figure 4. The change in JEBAR is highlighted to the Southern Ocean. This notable result is not immediately obvious from the top row illustrating the geographic locations of JEBAR in the experiments with 1° (left column), $1/4^\circ$ (middle column) and $1/12^\circ$ (right column) for from non-eddy resolving, intermediate to eddy-permitting resolution. The JEBAR term is associated with areas of roughness, and appear similar to the BPT term. The middle row of zonal area-averaged PDFs of each latitude highlights that the change in the JEBAR term is concentrated in the Southern Ocean. At non-eddy resolving 1° the kurtosis is similar at all latitudes. Increasing resolution produces increasingly widely distributed (low kurtosis) JEBAR PDFs, significantly pronounced in the Southern Ocean. The global area averaged PDF highlights the significant change with resolution in JEBAR that was not seen in the BPT term.

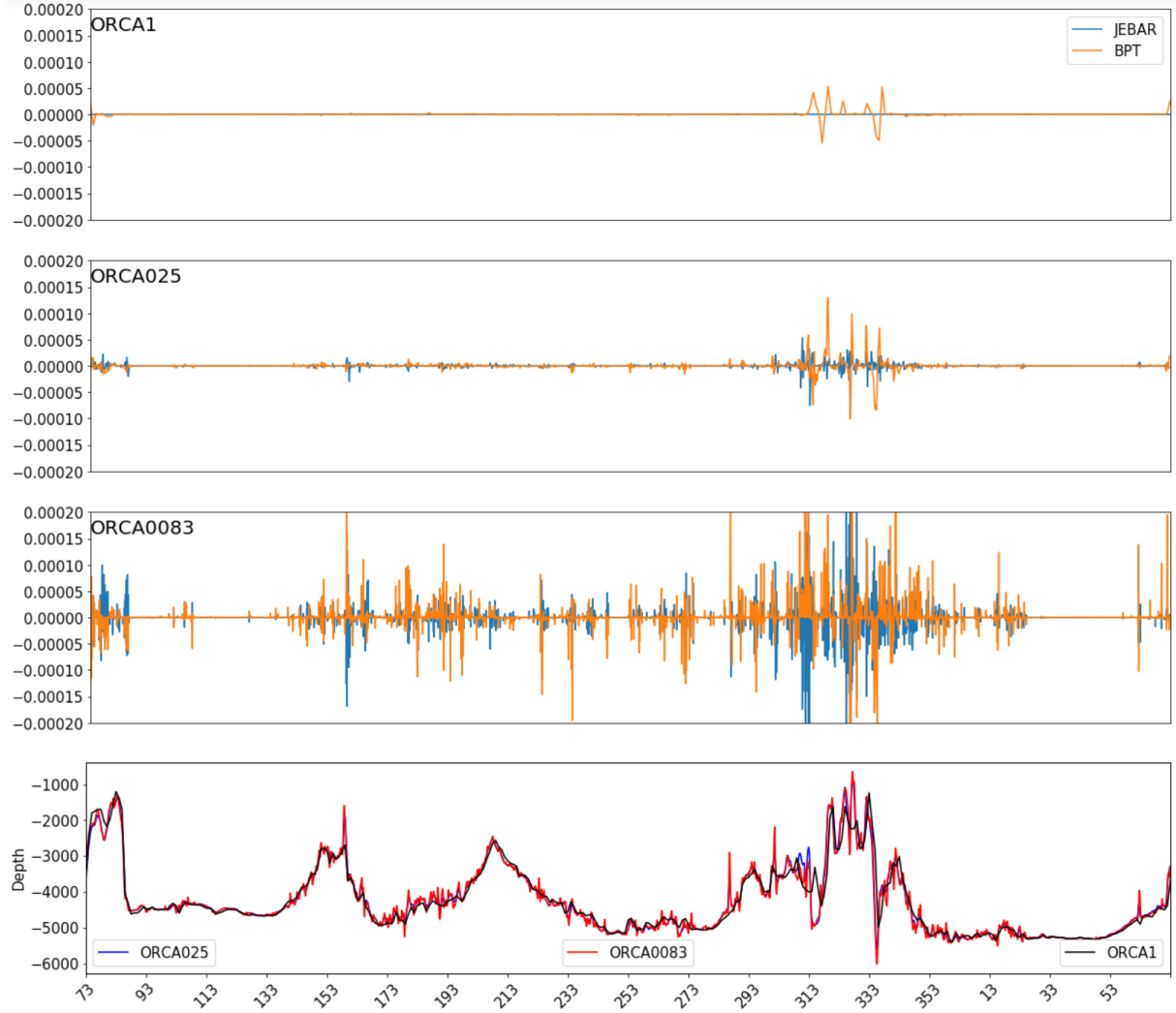


Figure 5. The JEBAR term is the baroclinic component of the BPT term, that highlights the importance of rough bathymetry and how resolving eddy scales influences the composition of the BPT term. At 60°S, no continents obstruct the path of the ACC. The bottom figure illustrates the depth profiles at 60°S for the 1° (blue), 1/4° (black) and 1/12° (red) for non-eddy resolving, intermediate to eddy-permitting resolutions. The upper panel illustrates the BPT (orange) and JEBAR (light blue) compensation for the non-eddy resolving 1°, concurrent with the illustrated bathymetry profile. The JEBAR term is very small, while the BPT is visible around areas where the bathymetry is rough. An increase in depth leads to positive BPT, while a decrease leads to negative BPT. The second panel down illustrates the intermediate 1/4° resolution, where the JEBAR term has a larger impact.

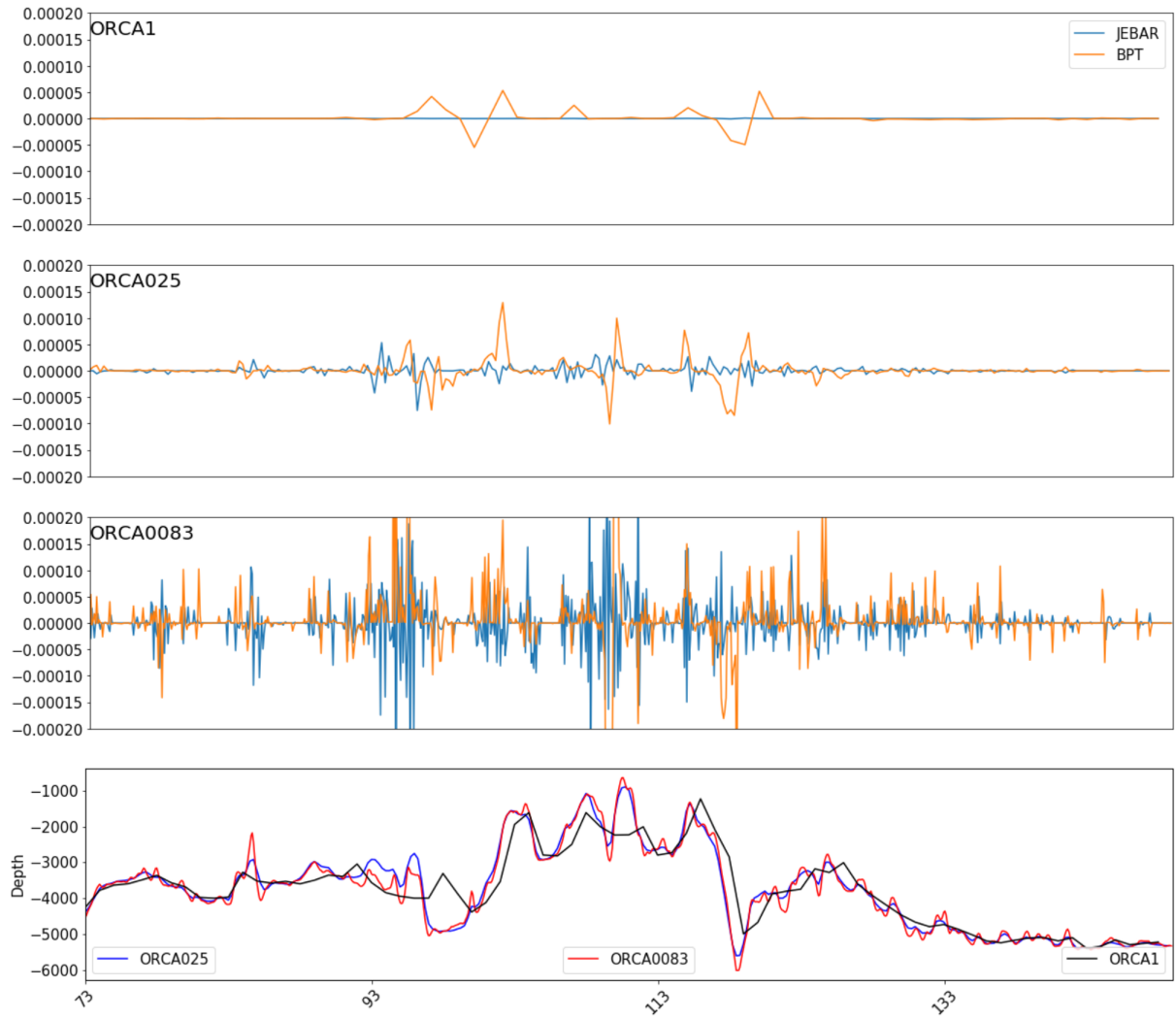


Figure 6. Detail of Fig. 5.

Name	ORCA1-N406	ORCA025-N401	ORCA0083-N01
Resolution	1°	1/4°	1/12°
z, x, y	75,292,362	75,1021,1442	75,3059,4322
GM active	Yes	No	No
Horiz. laplacian eddy viscosity ($m^2 s^{-1}$)	10^4	500	500
Horiz. bilaplacian eddy viscosity ($m^4 s^{-1}$)	-1.25×10^{10}	-2.2×10^{11}	-2.2×10^{11}
Lateral eddy tracer diffusivity ($m^2 s^{-1}$)	10^3	300	125
Timestep (s)	3600	1440	200

Table 1. Changes with resolution in configuration of NEMO. The vertical resolution (z) is at 75 vertical levels throughout the experiments.